J. Mech. Phys. Solids 213 (2026) 106637



Contents lists available at ScienceDirect

Journal of the Mechanics and Physics of Solids

journal homepage: www.elsevier.com/locate/jmps





Atomistic analysis of stress-dependent activation energy and dominant factors for dislocation nucleation from planar faults in BCC metals: A comparative study to FCC metals

Masato Wakeda [a,*], Tomohiro Ishigami [a,b], Takahito Ohmura [a,b]

[a] Research Center for Structural Materials, National Institute for Materials Science, 1-2-1 Sengen, Tsukuba, 305-0047, Japan
[b] Graduate School of Engineering, Kyushu University, 744 Motooka, Nishi-ku, Fukuoka, 819-0395, Japan

ARTICLE INFO

Keywords:
BCC
Atomistic simulation
Surface
Dislocation
Activation energy
Free energy

ABSTRACT

Dislocation nucleation from planar faults, such as grain boundaries and surfaces, is a fundamental plastic deformation event that influences the strength and fracture characteristics of polycrystalline metals and alloys. In this study, the free-end nudged elastic band method is used to determine the stress-dependent activation energy and dominant factors of dislocation nucleation, with edge and screw components, from surfaces (considered as planar faults) in body-centered cubic (BCC) metals. The energy barriers for dislocation nucleation in BCC metals mainly depend on Burgers vector and shear modulus, and they exceed those in FCC metals owing to the different nucleation morphology and affecting factors between BCC and FCC. For BCC Fe, an atomistically-informed model provides temperature and strain-rate-dependent stress for dislocation nucleation from a planar fault, enabling experimental comparison. The predictive model also shows the temperature- and shear stress-dependent frequency map of both dislocation nucleation from planar faults and kink-nucleation of pre-existing screw dislocations. The map indicates the necessity of a large shear stress for the dislocation nucleation and implies the dominant event depending on the dislocation density and applied shear stress. Free energy calculations also reveal temperature-dependent surface formation energy, which is a competitive event to dislocation nucleation at a crack tip under severe stress conditions, often discussed in ductile–brittle transition. The results provide the important fundamentals for dislocation-based modeling and design of BCC metals.

1. Introduction

Plastic deformation around grain boundaries (GBs) affects mechanical properties of polycrystalline metals. GBs affect yield stress of polycrystalline metals due to their ability to hinder dislocation glide motion or potency of dislocation nucleation sources (Kacher et al., 2014; Pan et al., 2021). Experimental studies involving analysis of the mechanical behavior of a single GB via nanoscale characterizations, such as nanoindentation, indicate that the GBs in body-centered cubic (BCC) metals are stronger obstacles than those in face-centered cubic (FCC) metals (Wang and Ngan, 2004). GB pop-in, correlated with dislocation pile-up and subsequent transmission across GB, is observed in nanoindentation experiments conducted on BCC metals; such phenomena are not detected in FCC metals

* Corresponding author.
E-mail address: wakeda.masato@nims.go.jp (M. Wakeda).

https://doi.org/10.1016/j.jmps.2026.106637
Received 28 December 2025; Received in revised form 10 April 2026; Accepted 13 April 2026
Available online 16 April 2026
0022-5096/© 2026 The Author(s). Published by Elsevier Ltd. This is an open access article under the CC BY license (http://creativecommons.org/licenses/by/4.0/).

(Javaid et al., 2021). Because obstacles to slip transfer in GBs include impeding glide motion of dislocations and suppressing dislocation generation in adjacent grains, evaluating the nucleation process is key to understanding GB strengthening. Dislocation nucleation around crack tips may affect fracture behavior (Rice and Thomson, 1974; Song and Curtin, 2013). Therefore, understanding dislocation nucleation from planar faults is fundamental for comprehending strengthening and fracture mechanisms of polycrystalline metals. Direct observation of dislocation nucleation from GBs or crack tips remains difficult due to small space- and time-scale. However, atomistic simulation effectively assesses nanoscale dislocation behaviors around GBs (Wakeda et al., 2021; Wakeda and Ohmura, 2023; Kura et al., 2022; Xu et al., 2016; Ma et al., 2022) and crack tips (Song and Curtin, 2013; Zhao et al., 2022). Recently, the activation energy and volume of dislocation nucleation from GBs and surfaces in FCC metals have been evaluated using atomistic simulations using the free-end nudged elastic band (FENEB) method (Zhang et al., 2016), which is useful for evaluating the energy barrier of dislocation nucleation (Zhang et al., 2022).

For FCC metals, molecular dynamics (MD) simulations have also been used to unveil the dynamics of dislocation nucleation (Kuhr et al., 2016; McPhie et al., 2012; Pan and Rupert, 2014; Liang et al., 2022). Numerous studies have provided atomistic knowledge on dislocation nucleation from planar faults in FCC metals. In contrast, fewer atomistic studies focus on dislocation nucleation in BCC metals (Sato et al., 2019; Wan et al., 2019) owing to the challenges associated with their simulations, given their large stacking fault (SF) energy and Peierls barrier. Thermally activated dislocation nucleation from GBs in BCC metals within MD time-scales is difficult due to the large SF energy and Peierls barrier. Therefore, additional techniques such as artificial introduction of dislocation loop are required. The dislocation nucleation from the GBs in realistic polycrystals depends on the GB character (e.g., tilt, twist, or random GB), shape of the GB plane, grain size, and complex stress fields around the GB, including the stress concentration mechanism. Due to these factors, revealing the features of dislocation nucleation from the GBs in BCC metals via comparisons with those in FCC metals using experiments and atomistic simulations remains challenging.

In this study, we evaluated the energetic information and dominant factors of dislocation nucleation from BCC surfaces under various stress levels to simplify the influencing factors. To provide a general discussion of BCC metals, we evaluated the dislocation nucleation in BCC Fe, Ta, and W, which have different lattice constants, shear moduli, and generalized SF energies. For comparison, the dislocation nucleation in FCC Cu and Ni was examined as well to assess the differences between BCC and FCC metals. Because the line tension of the screw component is much higher than that of the edge component in BCC metals (Hirth and Lothe, 1982; Blaschke and

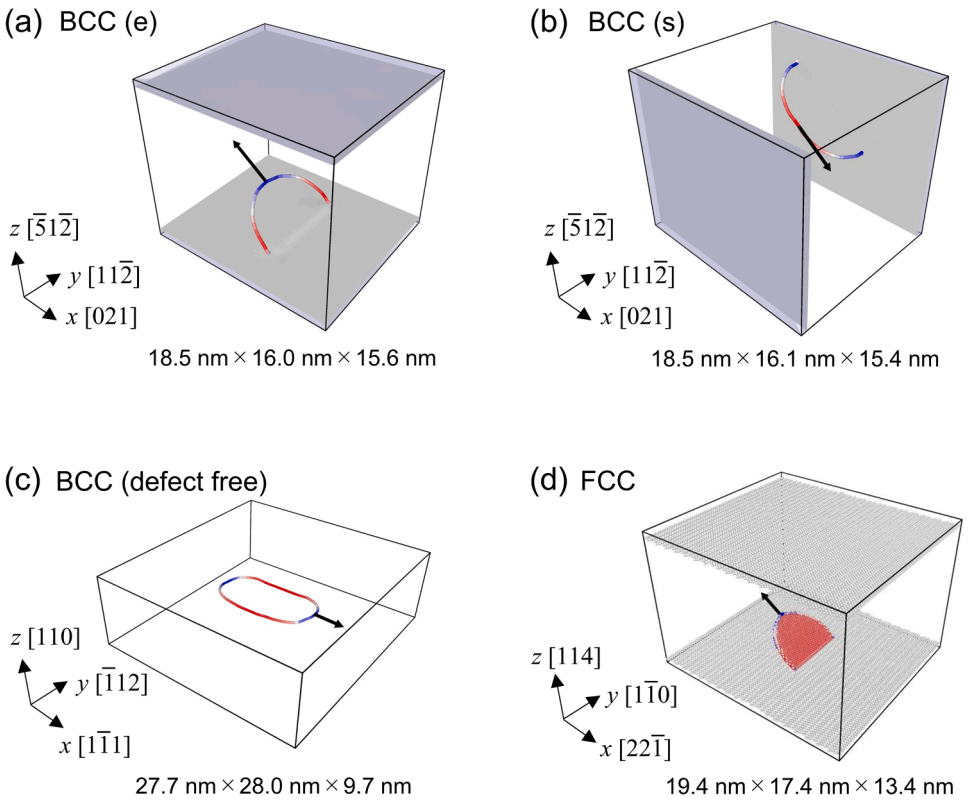


Fig. 1. Atomic model of dislocation nucleation FENEB analyses. Nucleation of (a) edge-type from the surface in BCC Fe, (b) screw-type from the surface in BCC Fe, (c) dislocation whole loop in defect-free region of BCC Fe, and (d) edge-type from the surface in FCC Ni. The black arrow represents slip direction. Dislocation is detected by DXA analysis (Stukowski and Able, 2010). The blue and red dislocation line represents the edge and screw components, respectively. In (d), the red atom means HCP configuration (i.e., SF region), while the white atom means structure other than BCC, FCC, HCP, and Icosahedron (i.e., surface). The crystallographic orientation and model size along *x*, *y*, and *z* directions are depicted in each figure. The model in (a) and (d) has a surface perpendicular to the *z* direction, while the model in (b) has a surface perpendicular to the *y* direction.

Szajewski, 2018), we evaluated the effects of dislocation type (edge or screw) on the activation energy and volume. Based on the obtained relationship between activation energy and applied stress for BCC Fe, we constructed an atomistically-informed predictive model for dislocation nucleation stress. We comparatively showed the frequency of dislocation nucleation and pre-existing dislocation motion contributing to plastic deformation. We performed free energy calculations to determine the temperature effects on the surface formation energy, which is related to brittle fracture. These results revealed energetic information and dominant factors for dislocation nucleation near planar faults (surfaces and GBs) under various temperatures and provided the fundamentals for strengthening and fracture mechanisms of BCC metals.

2. Materials and methods

MD and FENEB simulations were conducted using the embedded atom method (EAM) potentials. This study qualitatively reveals the differences in the activation energy and volume of the dislocation nucleation between (i) BCC and FCC, (ii) edge and screw components in BCC, and (iii) the surface and defect-free regions of BCC. The EAM potentials for BCC Fe (Mendelev et al., 2003), BCC Ta (Ravelo et al., 2013), BCC W (Marinica et al., 2013), FCC Cu (Mishin et al., 2001), and FCC Ni (Mishin et al., 1999) employed in this study have been used in previous dislocation analyses. For BCC Fe, we also used a neural network potential (NNP) developed by Mori et al. (Mori and Ozaki, 2020; Mori et al., 2023). In general, NNPs outperform EAM potentials in terms of accuracy. A comparison between the EAM and NNP results for BCC Fe confirms that the employed EAM systems are reasonable for the present dislocation nucleation analyses. Fig. 1(a) and (b) show the atomistic model for the analysis of dislocation nucleation from the surface in BCC. In Fig. 1(a) and (b), when the dislocation becomes sufficiently straight and parallel to the surface after the dislocation nucleation and propagation, the dislocation component becomes a pure edge and pure screw, respectively; therefore, the dislocation nucleation are referred to as "edge type" and "screw type" (also denoted by "(e)" and "(s)"), respectively; the blue lines in the figure represent the edge component, and the red ones mark the screw component. Fig. 1(c) shows the dislocation nucleation as a loop shape from lattice interior in the defect-free region of BCC Fe. Fig. 1(c) compares the dislocation nucleation between the surface and defect-free region to clarify the effect of the surface on the dislocation nucleation. Fig. 1(d) shows the dislocation nucleation from the surface in FCC. As evident from Fig. 1(d), sufficiently after a dislocation nucleation and propagation, a straight dislocation parallel to the surface becomes a pure edge (i.e., edge type). Table 1 lists the properties of the metals calculated using the EAM potentials and NNP employed. For BCC metals, the lattice constant a, Burgers vector b, shear modulus μ, and maximum value of the generalized SF energy of the slip system of {110}<111>, γ_{max} are presented. For FCC metals, the lattice constant a, Burgers vector b, shear modulus μ, intrinsic SF energy γ_{isf}, and unstable SF energy γ_{usf} are presented. The shear moduli were calculated via simple shear simulations of the crystalline models without a dislocation and a surface (i.e., bulk models); {shear plane}<shear direction > for the BCC and FCC models were {110}<111 > and {111}<112>, respectively. We calculated γ_{max} of the {110} plane by sliding the plane along the ⟨111⟩ direction for BCC metals. Meanwhile, for FCC metals, the energies of the intrinsic and unstable SFs on the {111} plane were calculated by sliding the plane along the ⟨112⟩ direction via displacements of 1/6 < 112 > and 1/12 < 112>, respectively (Kibey et al., 2006; Li et al., 2022).

Prior to the FENEB analyses of the dislocation nucleation from the surface, we conducted uniaxial tensile MD simulations at 10 K along the x-axis to construct atomic models with varying stress values along the loading axis. The model dimensions along the y direction in Fig. 1(a) and z direction in Fig. 1(b) were controlled to maintain zero-external stress conditions. The normal stress along the z direction in Fig. 1(a) and the y direction in Fig. 1(b) is always zero owing to the free-surface conditions. For the snapshots obtained by uniaxial simulation, we conducted instantaneous quenching using the conjugate gradient (CG) method at zero kelvin. We introduced a dislocation half-loop near the free surface of the atomic configuration after instantaneous quenching, wherein the slip system was {110}<111 > . Subsequently, FENEB analysis was conducted to evaluate the energy barrier for dislocation nucleation. The number of images, including the initial and the final images, is 21. Similar to the BCC metals, for the FCC metals, MD uniaxial tensile simulations, CG simulations, and dislocation introductions were performed to prepare the FENEB analysis of dislocation nucleation from the surface. The slip system in the FCC models was {111}<112> (Fig. 1(d)). For the dislocation nucleation in the defect-free region of BCC Fe, we prepared atomic models and introduced a dislocation loop under periodic boundary conditions in all orthogonal directions. The slip system was {110}<111 > . To evaluate the effect of applied stress, we conducted FENEB simulations of the dislocation nucleation from the surface in BCC (Fe, Ta, and W) and FCC (Cu and Ni) metals under different uniaxial loading states (loading direction is x-axis) and that in the defect-free region of BCC Fe under different simple shear deformation (shear direction is ε_{zx}). We employed the LAMMPS code (Thompson et al., 2022) for the MD simulations and Ovito (Stukowski, 2009) for visualization of dislocations in metals.

Table 1
Properties of metals calculated by the employed interatomic interactions. The Burgers vector of BCC system corresponds to the general {110}<111 > slip system.

	a (Å)	b (Å)	μ (GPa)	γ_{max} (J/m^2)	γ_{usf} (J/m^2)	γ_{isf} (J/m^2)
Fe	2.86	2.47	71.5	0.66	–	–
Fe (NNP)	2.84	2.46	79.7	0.98		
W	3.14	2.72	160.4	1.53	–	–
Ta	3.30	2.86	61.2	0.95	–	–
Ni	3.52	2.49	77.6	–	0.37	0.13
Cu	3.62	2.56	41.2	–	0.16	0.04

3. Results

Fig. 2(a) shows the energy profiles of dislocation nucleation under different applied stress states (here, we present the edge-type nucleation in BCC Fe calculated by EAM potential as an example). The peak height of each curve represents the energy barrier for dislocation nucleation. The energy barrier for dislocation nucleation decreased with increasing applied shear stress. In Fig. 2(b), snapshots of states (i)–(iv) of Fig. 2(a) are shown. State (ii) is the saddle point at which the energy profile had maximum energy. From all the energy profiles, we obtained the energy barriers and summarized them in Fig. 2(c), where the horizontal axis represents the shear stress acting on the dislocation slip system (i.e., resolved shear stress) denoted by τ and the vertical axis is the energy barrier (i.e., saddle point energy) denoted by $E(\tau)$. For $E(\tau)$ and τ relations obtained by the FENEB analyses, we fitted the Kocks' law in the form of $E(\tau) = A[1\text{-}(\tau/\tau_{ath})^p]^q$ and obtained the fitting parameters A, p, q, and τ_{ath}. The fitting parameters of Kocks' law are summarized in Table S1 in Supplementary Materials. Using Kocks' law equation and fitting results, the activation volume Ω was obtained by $\Omega = -\partial E(\tau)/\partial\tau$. The relationship between Ω and τ for edge-type nucleation in BCC Fe is shown in Fig. 2(d); the activation volume decreased with increasing τ.

For the BCC (Fe, Ta, and W) and FCC (Cu and Ni) metals, the activation energy of dislocation nucleation from the surface as a function of the resolved shear stress are summarized in Fig. 3(a). The relationship between the activation energy and the resolved shear stress is dependent on the elements and crystalline structures. For instance, BCC W requires a larger resolved shear stress than other metals in case of an equivalent energy barrier. This result indicates that the dislocation nucleation from the surface in BCC W is much more difficult than that of the other BCC and FCC metals calculated in this study. In addition, the screw type exhibited a slightly higher activation energy than the edge type for BCC Fe, Ta, and W. BCC Fe exhibits a larger activation energy than FCC Ni, although BCC Fe

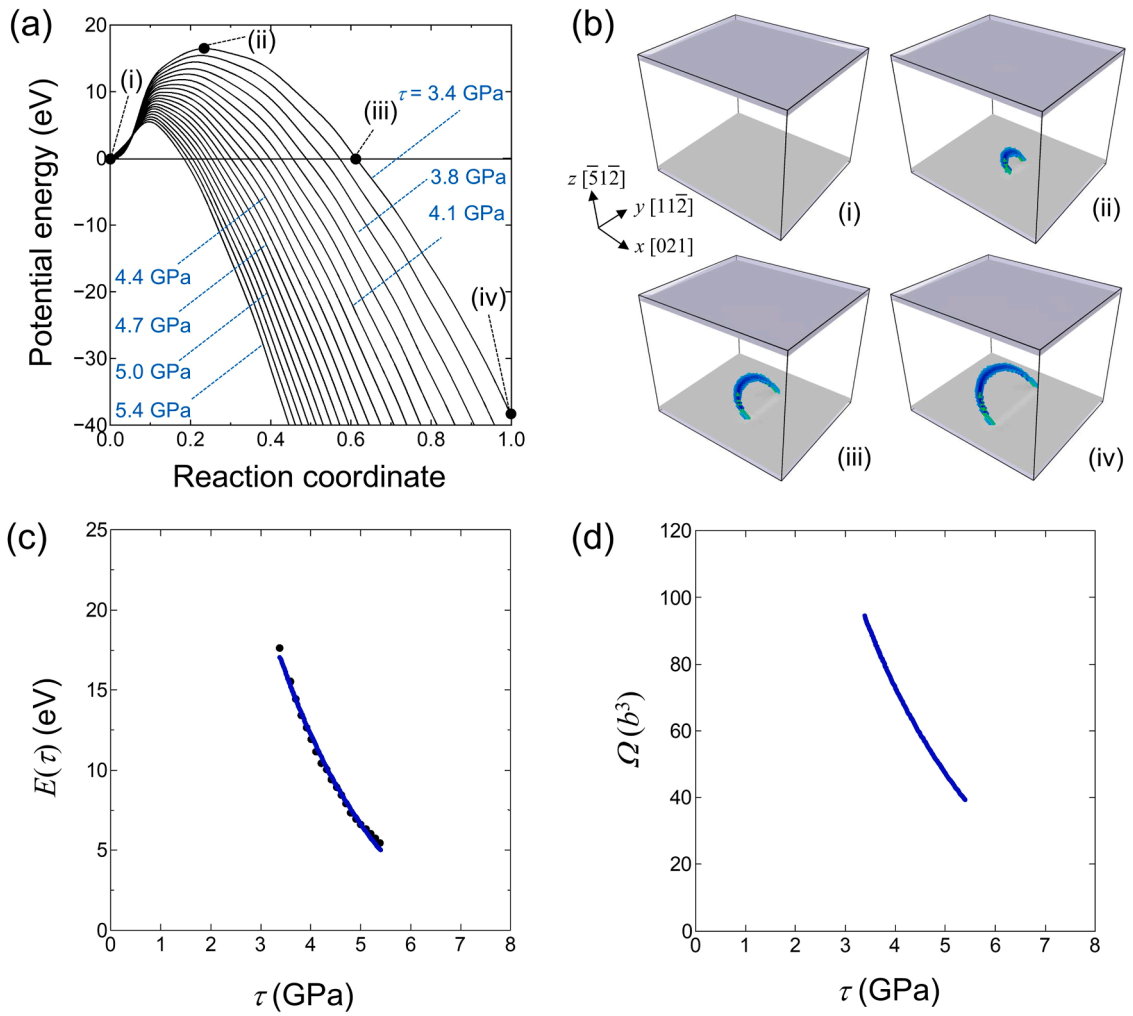


Fig. 2. (a) Energy vs. reaction coordinate of dislocation nucleation calculated by FENEB with EAM potential for BCC Fe. The same figure with NEB plots can be seen in Fig. S1 in Supplementary Materials. The atomic model of state (i)-(iv) on the energy profile (τ =3.4 GPa) in (a) is shown in (b). (c) Activation energy vs. resolved shear stress (marks represent FENEB results, and blue line represents fitting curve by Kock's law). (d) Calculated activation volume as a function of resolved shear stress. All panels (a), (b), (c), and (d) are edge-type nucleation from the surface in BCC Fe.

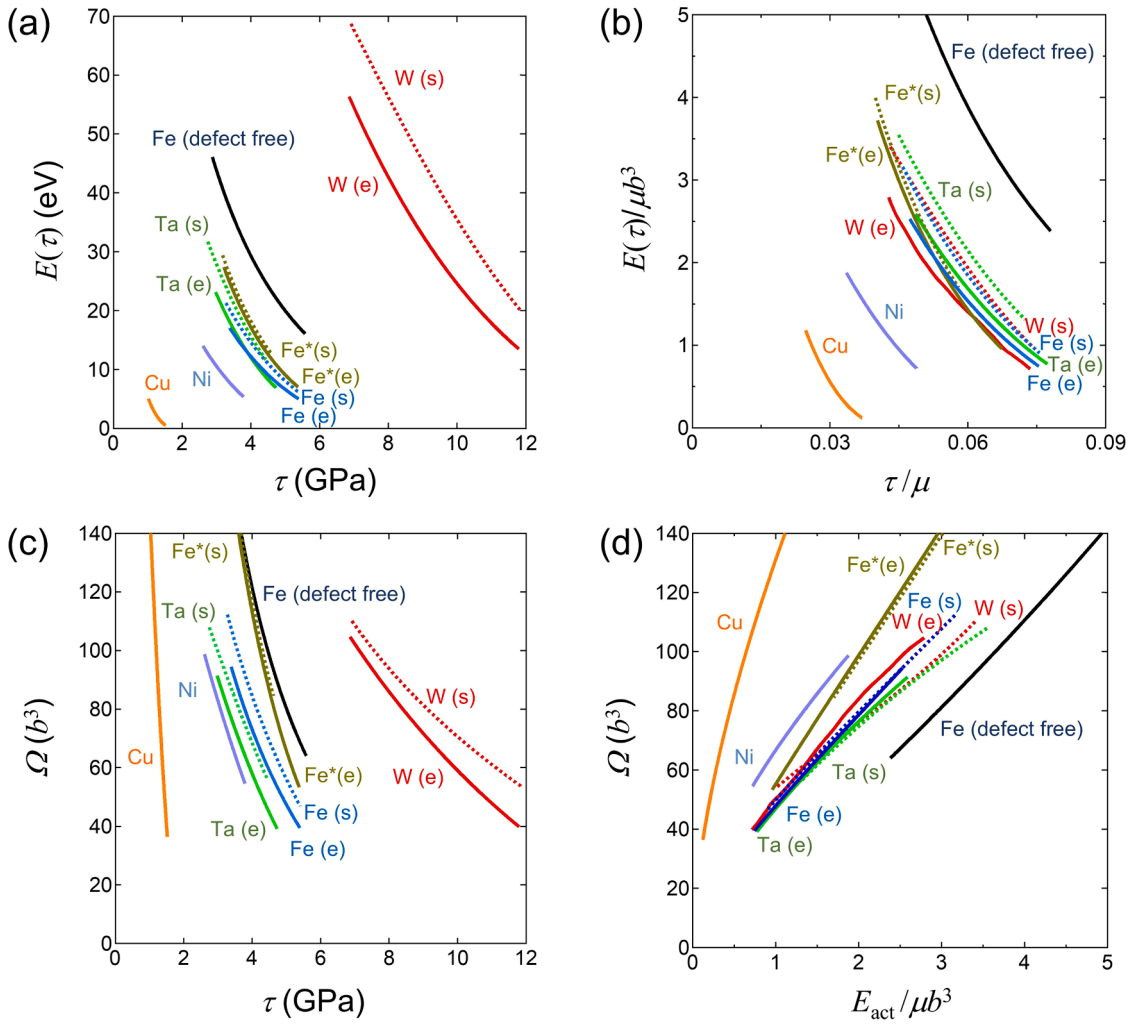


Fig. 3. (a) Activation energy vs. resolved shear stress, (b) normalized activation energy vs. normalized resolved shear stress, (c) activation volume vs. resolved shear stress, and (d) activation volume vs. normalized activation energy for various BCC and FCC metals. We also show the results of dislocation loop nucleation in defect-free region of BCC Fe. In the case of dislocation nucleation from the surface of BCC metals, solid and broken curves represent edge and screw types (denoted by (e) and (s) in the figures), respectively. "Fe" and "Fe*" in each panel represent the results calculated using EAM potentials and NNPs, respectively.

and FCC Ni have similar Burgers vector and shear modulus. We normalized the activation energy and resolved shear stress because Fe, Ta, W, Cu, and Ni have different shear moduli and Burgers vectors. Figure 3(b) shows the normalized activation energy vs. normalized resolved shear stress. The activation energy was normalized by μb^3, which has the unit of energy. Interestingly, the normalized curves of BCC Fe, Ta, and W were located at similar positions and were higher than those of FCC Cu and Ni. Activation energy as a function of normalized resolved shear stress is also shown in Fig. S2(a) in Supplementary Materials. Figure 3(b) suggests the activation energies for dislocation nucleation in BCC metals depend on Burgers vector and shear modulus rather than the stacking fault energy and Peierls potential. This is different from the dislocation nucleation from FCC metals, which also depend on the stacking fault energy (Zhang et al., 2022). This is attributed to the difference in their morphology of dislocation nucleation; in BCC metals, dislocation nucleation has a component of perfect dislocation, whereas in FCC metals, is originates from partial dislocations and the SF region as discussed later. Figs. 3(a), (b), and Fig. S2(a) suggest that the dislocation nucleation from the surface in BCC Fe, Ta, and W requires a larger energy barrier (or a larger resolved shear stress) than that of FCC Cu and Ni. In addition, as shown in Figs. 3(a), (b), and Fig. S2(a), the energy barrier of the dislocation nucleation in the defect-free region of BCC Fe was much larger than that of the dislocation nucleation from the surface in BCC Fe. The dislocation nucleation in the defect-free region of the BCC metal occurs in the shape of a complete loop (i.e., not a half-loop), which requires a larger energy barrier than that of the nucleation of a half-loop from the surface. As the dislocation nucleation from the GB also has a half-loop shape similar to that of the surface (Aifantis et al., 2019; Yao et al., 2021), the energy barrier for the dislocation nucleation from the GB should be smaller than that from the defect-free region. Experimental studies on nanoindentation have indicated that the dislocation nucleation from the GBs requires a smaller load than that in the grain interior

(Ohmura et al., 2005).

Fig. 3(c) shows the activation volumes of the BCC metals (Fe, Ta, and W) and FCC metals (Cu and Ni) as a function of the resolved shear stress. Activation volume as a function of normalized resolved shear stress is also shown in Fig. S2(b) in Supplementary Materials. In all BCC cases (i.e., Fe, Ta, and W), the activation volume of the screw-type nucleation was slightly larger than that of the edge-type nucleation. This trend is consistent with the activation energies shown in Figs. 3(a), (b), and Fig. S2(a) because a large activation volume generally requires a large energy barrier. The relationship between the normalized activation energy and activation volume is shown in Fig. 3(d), wherein the activation volume increased with an increase in the normalized activation energy. Figure 3(d) implies that the relationship between the normalized activation energy and activation volume depends on the morphology of the dislocation nucleation.

Fig. 4 shows the morphology of (a) edge-type nucleation from the surface in BCC Fe, (b) screw-type nucleation from the surface in BCC Fe, (c) dislocation loop nucleation in the defect-free region of BCC Fe, and (d) edge-type nucleation from the surface in FCC Ni. The dislocation shape at the saddle point is also indicated by the scale bars. At the saddle point, the dislocation in the BCC metals is a perfect dislocation with a half or whole loop, as shown in Figs. 4(a), (b), and (c). By contrast, the dislocation in the FCC metals is composed of partial dislocations and SF regions, as shown in Fig. 4(d). This difference between the dislocation nucleation morphologies of the BCC and FCC metals is attributed to the SF energies. Because the SF energy of FCC metals is lower than that of BCC metals, the dislocation core structure decomposes into partial dislocations and SF regions. Therefore, dislocation nucleation in FCC metals can be realized by the leading partial dislocation and SF regions. This nucleation morphology in FCC metals reduces the energy barrier for nucleation. Notably, at the saddle point, the dislocation line length in the defect-free BCC Fe model is larger than that in the BCC Fe surface model. This discrepancy is the origin of the energy barrier for dislocation nucleation in the defect-free BCC Fe model being larger than that in the surface model (Fig. 3).

Experimental studies indicate that compared to the GBs in FCC metals, the GBs in BCC metals strongly hinder deformation transmission through them (as described in Section 1) (Wang and Ngan, 2004; Javaid et al., 2021). The dislocation nucleation from GBs, or that at a source site around GBs, is a well-discussed part of deformation transmission process. Figures 3(a) and (b) suggest that the resolved shear stress for dislocation nucleation from the surface in BCC metals is larger than that in FCC metals because of the high SF energy of the former. In the case of small activation volumes, the dislocation nucleation in BCC and FCC metals should be dominated by γ_{max} and γ_{usf}, respectively. In such cases, the barrier for dislocation nucleation also should be higher in BCC metals than in FCC

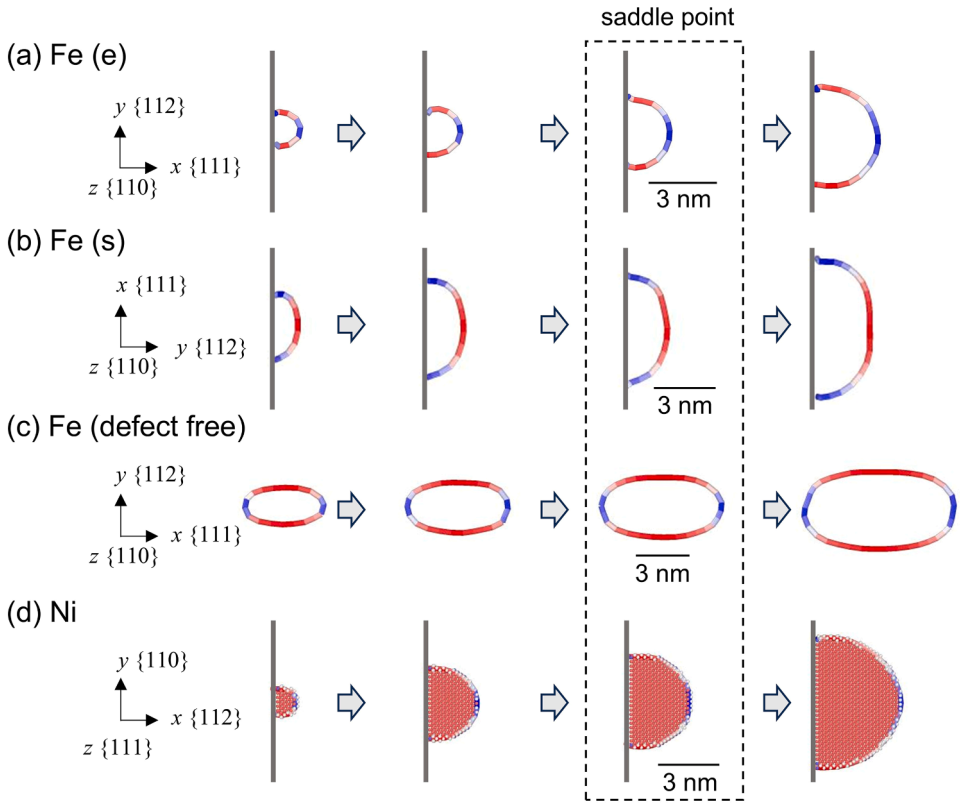


Fig. 4. Nucleation behaviors of (a) edge-type from the surface in BCC Fe calculated by EAM potential, (b) screw-type from the surface in BCC Fe, (c) dislocation loop in defect-free region of BCC Fe, and (d) edge-type from the surface in FCC Ni. Images surrounded by a dotted rectangular represent dislocation shapes at the saddle point with scale bars. In (a), (b), and (d), we added vertical lines to show the free surface position. In (d), red atoms represent SF region. The blue and red dislocation line represents the edge and screw components, respectively.

metals (Table 1). Although the dislocation transmission across GBs is affected by various factors, such as dislocation pile-up and dislocation absorption at the GBs, the large energy barrier for the dislocation nucleation in BCC metals can be one of the possible factors of the relatively large barrier for deformation transmission in these metals.

Figure 5(a) shows the morphology of the edge- and screw-type nucleation at the saddle point, where the dislocation exhibits a half-loop shape composed of both edge and screw components. In BCC metals, the line tension of the screw component is significantly greater than that of the edge component (Hirth and Lothe, 1982; Blaschke and Szajewski, 2018). Owing to the difference in the line tension, the dislocations in Fig. 5(a) exhibit a half-elliptical shape with a long screw segment. In a previous study, we investigated the dislocation transmission across low-angle GBs (i.e., GBs with a small misorientation angle) and revealed that screw dislocations required a much larger shear stress for transmission than edge dislocations owing to the large line tension of the screw component (Wakeda and Ohmura, 2023). In a previous study (Wakeda and Ohmura, 2023), transmission occurred by the bowing out of a short dislocation segment, both ends of which were pinned by GB dislocations. Therefore, dislocation transmission in low-angle GBs is dominated by the Orowan bowing-out process, wherein the line tension is an important factor. However, the dislocation nucleation from the surface in this study did not have pinning points at the surface. Therefore, the activation energies of the edge and screw types were similar in magnitude, although the screw type exhibited a slightly larger energy barrier than the edge type, as shown in Figs. 3(a), (b), and Fig. S2(a).

Dislocation nucleation from surface makes changes of atomistic structure and energy of the surface. To provide the information on the contributing factors of the energy barrier for dislocation nucleation, the activation energy was discretized into two parts: (i) the dislocation self-energy of a half-loop and energy change attributed to stress relaxation by dislocation nucleation; (ii) energy changes at the surface. In this study, the former energy was calculated from the region located more than 5 Å from the surface, whereas the latter energy was calculated from the region located less than 5 Å from the surface. The total activation energy and discretized activation energies are shown in Fig. 5(b). Regarding the former (i), the dislocation self-energy increases, while the stress relaxation decreases the energy barrier for dislocation nucleation. The total activation energy of screw-type nucleation is higher than that of edge-type nucleation in BCC iron (EAM) (as already shown in Figs. 3(a), (b), and Fig. S2(a)). This agrees with Fig. 5(b), where the former (i) of screw-type is slightly higher than that of edge-type. The stress relaxation effects mainly depend on the length of the dislocation component and may affect a similar contribution in both edge and screw types. In the present simulation, a small reduction of stress components caused by the dislocation nucleation was observed. In addition, regarding latter (ii), the energy change at the surface differs between the screw- and edge-types. Figure 5(c) shows the distribution of the change in potential energy at the surface owing to dislocation nucleation. This energy change at the surface depends on the surface structure and nucleated dislocation type (edge, screw,

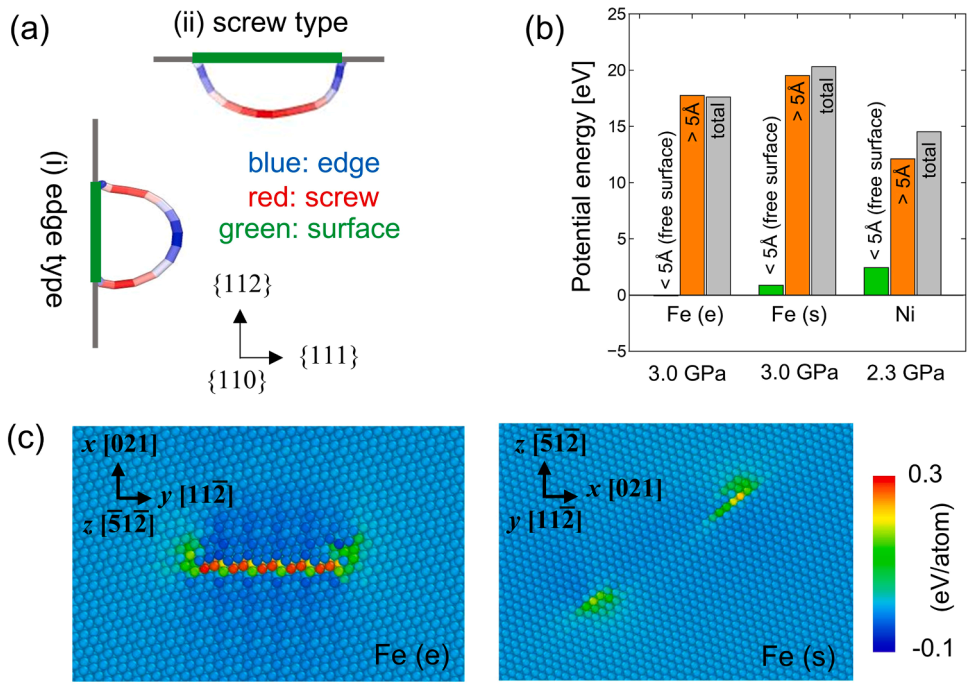


Fig. 5. (a) Saddle point structure of edge- and screw-type nucleation from the surface in BCC Fe calculated by EAM potential. (b) Discretized nucleation energy of edge- and screw-type in BCC Fe and edge-type in FCC Ni. Energy barrier for dislocation nucleation are 17.6 eV (edge-type in BCC Fe), 20.1 eV (screw-type in BCC Fe), and 14.6 eV (edge-type in FCC Ni). The resolved shear stresses are also depicted below the graph. (c) Distribution of energy change at the surface by dislocation nucleation at saddle point state of edge and screw types in BCC Fe. Note that the surface energies of $[\bar{5}1\bar{2}]$ plane in BCC Fe (i.e., surface of Fig. 1(a)), $[11\bar{2}]$ plane in BCC Fe (i.e., surface of Fig. 1(b)), and [114] plane in FCC Ni (i.e., surface of Fig. 1(d)) before dislocation nucleation are calculated as 1.90, 1.92, and 2.06 J/m^2, respectively. These values were calculated by EAM potentials.

and mixed). For instance, the discretized energy change due to dislocation nucleation in the case of FCC Ni (i.e., edge-type nucleation) is considerable at the surface, as shown in Fig. 5(b). In Fig. 5(b), when comparing the edge- and screw-type of BCC Fe, the edge-type exhibits a smaller energy change at the surface. In Fig. 5(c), the atomic-scale positive and negative energy changes in the case of the edge-type can be seen; the sum of them becomes almost zero. On the other hand, the screw-type basically induces a positive atomic-scale energy change at the surface, resulting in a larger energy change at the surface than the edge-type, as shown in Fig. 5(b). Note that the contribution of energy change depends on the surface roughness and the crystallographic orientation of the surface. Therefore, for a better understanding, systematic analyses of various surface structures are required, and this may be future work.

Based on the results shown in Fig. 3(a), we predict the necessary shear stress for dislocation nucleation at a given temperature and strain rate. The cumulative probability of dislocation nucleation can be estimated as

$$f = 1 - \exp\left[-\int_0^{t_c} k(\tau, T)dt \right], \tag{1}$$

where τ is the applied shear stress, and t_c is the time at which f becomes 0.5. Using the strain rate $\dot{\gamma}$ and shear modulus μ (see Fig. S3 in Supplementary Materials), the shear stress, at which f becomes 0.5, can be defined as $\tau = \mu\dot{\gamma}t$ and $\tau_c = \mu\dot{\gamma}t_c$, respectively. Based on the transition state theory, the dislocation nucleation rate, $k(\tau, T)$, can be represented as

$$k(\tau, T) = N_{site} k_0 \exp\left(-\frac{G(\tau,\ T)}{k_B T} \right), \tag{2}$$

where N_{site} is the number of possible nucleation sites, k_0 is the attempt frequency, k_B is the Boltzmann constant, T is the temperature, and $G(\tau,\ T)$ is the activation free energy. The activation free energy is calculated as

$$G(\tau,\ T) = E(\tau)\left(1 - \frac{T}{T_m} \right), \tag{3}$$

where $E(\tau)$ is the energy barrier for edge dislocation nucleation as a function of τ (i.e., a fitted curve obtained from Fig. 3(a)), and T_m is the surface melting temperature. Using these equations, we estimate the critical shear stress for dislocation nucleation, τ_c, at which $f =$ 0.5. Fig. 6 shows τ_c derived as functions of temperature and strain rate for BCC Fe using NNPs with $N_{site} = 10^3$, $k_0 = 10^{13}$ s^{-1} (Fan et al., 2012), and T_m is one-half of the bulk melting temperature (1811 K). Calculations with the N_{site} values —which depend on the surface structure and stress concentration—, of 10^1 and 10^6 are also shown for comparison (Fig. S4 in Supplementary Materials).

Fig. 6 suggests that the necessary shear stress for dislocation nucleation, τ_c, at room temperature and a strain rate of 1 s^{-1}, is ~7.6 GPa. τ_c decreases with increasing temperature and decreasing strain rate. In the calculated ranges, the temperature effect dominates over that of the strain rate. In experimental nanoindentation for BCC Fe, the estimated shear stress for dislocation nucleation is 9.2 GPa (Ohmura et al., 2012). Although the present simulation treats dislocation nucleation from the surface, the simulated order of shear stress for dislocation nucleation is similar to that observed experimentally. Dislocation nucleation occurs both from surfaces and GBs, with the dislocation featuring a half-loop shape at the saddle point. This result validates our estimated critical stress for dislocation nucleation.

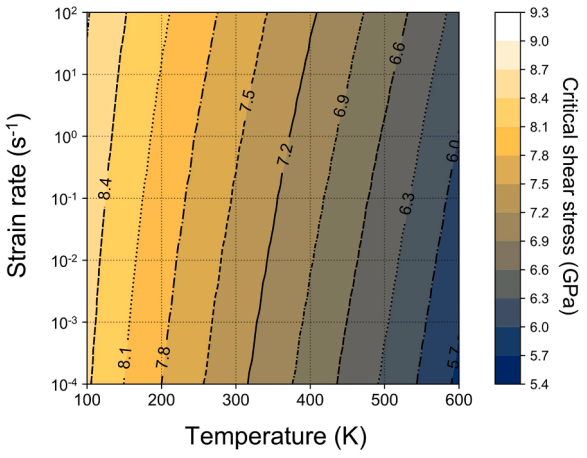


Fig. 6. Theoretically predicted critical shear stress for dislocation nucleation. The energy barrier for dislocation nucleation is calculated using NNPs for BCC Fe (see Fig. 3(a)).

4. Discussion

Non-Schmid effect on the dislocation glide motion in the BCC system has been investigated in experimental (Argon and Maloof, 1996; Spitzig and Keh, 1970) and computational (Ito and Vitek, 2001; Kraych et al., 2019) studies. The effect has been discussed as the origin of tension/compression asymmetry. Recently, an atomic study based on the first-principles calculation suggested that the effect originates from the screw dislocation core field and the glide motion. We here evaluated the effect of non-glide stress components on the energy barrier for dislocation nucleation using the defect-free BCC Fe model with EAM potential (see Fig. S5 and related explanations in Supplementary Materials). In the case of the energy barrier for dislocation nucleation, we observed no significant impact of non-glide stresses on the dislocation nucleation. The energy barrier for dislocation nucleation is much larger than that for dislocation motion, and this may be a major reason for the small effect of non-glide stresses.

The Orowan equation, $\dot{\varepsilon}_p = \rho_m b v$, suggests that the plastic strain rate is related to mobile dislocation density (ρ_m) and dislocation velocity (v). In the presence of a sufficient number of pre-existing dislocations in grain interiors, the dislocation motion can satisfy the applied strain rate. Meanwhile, if the dislocations density is significantly low, such as the cases of nanopillars and polycrystals with nanoscale grains, dislocation nucleation from surfaces or GBs is reasonably expected. In other words, dislocation nucleation is also significantly affected by the dislocation mobility and pre-existing dislocation density. In this study, we can theoretically evaluate the competition between the dislocation mobility in the grain interior and the dislocation nucleation from the surface, which should be used as the basis for predicting dislocation-related plastic events in BCC Fe, such as nanopillars. Regarding dislocation mobility, we evaluate the kink-pair formation frequency of screw dislocations because in BCC Fe, the kink-pair formation dominates the screw dislocation velocity rather than the kink migration in the absence of solute species (Wakeda et al., 2017). Notably, the mobility of edge dislocations is larger than that of their screw counterparts. The kink-pair formation frequency of screw dislocations can be represented by $k_{kn}\exp\{-G_{kn}(\tau, T)/(k_B T)\}$, where k_{kn} denotes the attempt frequency, and $G_{kn}(\tau, T) = E_{kn}(\tau)(1 - T/T_m)$ is the activation free energy for kink-pair formation. In the present calculations, we set $k_{kn} = 2 \times 10^{10}$ s^{-1} and apply the $E_{kn}(\tau)$ value obtained in our previous study based on EAM potentials (Shinzato et al., 2019). For the edge dislocation nucleation frequency, we use Eq. (2) and the parameters for dislocation nucleation obtained using the NNPs. Fig. 7 shows the frequencies of kink-pair formation in the grain interior and of edge dislocation nucleation from the surface at various temperatures. A sufficient number of kink pairs can form at stresses lower than 1 GPa, whereas dislocation nucleation from the surface requires significantly high stresses. This result demonstrates that in the presence of a sufficiently high dislocation density, pre-existing dislocations play a dominant role in plastic deformation. Conversely, if few dislocations exist, forming a starvation state in the grain interior, such as a nanopillar, then dislocation nucleation is induced by applying a high stress; similar phenomenon is observed in experiments (Sekido et al., 2012).

As discussed in Figs. 6 and 7, dislocation nucleation requires a high-stress state that can be typically realized at a crack tip. Under a high-stress state at a crack tip, dislocation nucleation (i.e., plastic deformation) often suppresses surface nucleation at the crack tip (i.e., crack propagation) due to relaxation of stress concentration, rounding of the crack tip, and back stress of the dislocations that have been previously emitted. Fig. 6 shows the temperature and strain-rate-dependent necessary stress for dislocation nucleation. For comparison, the temperature-dependent surface formation free energy is shown as well. Using Frenkel-Ladd method, we evaluated the surface formation free energy (γ_s) of the $(\bar{5}1\bar{2})$ plane, which was used to determine the energy barrier and necessary shear stress for edge dislocation nucleation in this study. Notably, $(\bar{5}1\bar{2})$ plane does not represent a general fracture plane in BCC metals. Fig. 8 demonstrates that the surface formation free energy, evaluated from 100 K to 600 K using the thermodynamic integration method (Freitas et al., 2016; Koning and Antonelli, 1996), gradually decreases with increasing temperature. The temperature-dependent critical stress intensity factor for crack propagation K_G can be calculated by $\sqrt{2E\gamma_s/(1-\nu^2)}$, where E, γ_s, and ν represent Young's modulus, the surface formation energy, and Possison's ratio, respectively (Suzudo et al., 2022). A low K_G implies easy crack propagation. The dislocation nucleation discussed in the present study is a thermally activated process, whereas the temperature effect on

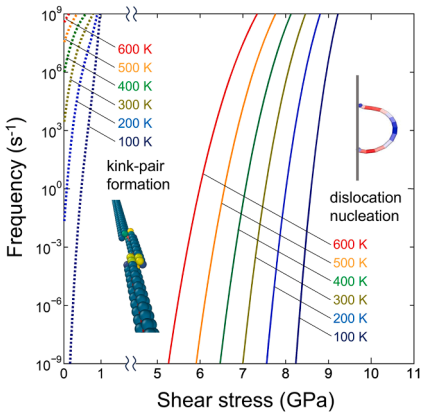


Fig. 7. Atomistically-informed frequency of a kink-pair formation on a screw dislocation in the grain interior and an edge dislocation nucleation from a surface in BCC Fe.

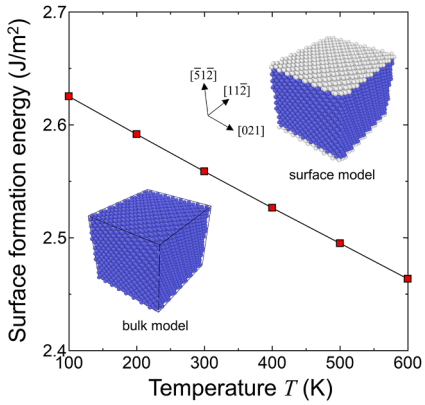


Fig. 8. Temperature dependencies of surface formation free energy for the $(\bar{5}1\bar{2})$ plane in BCC Fe (NNP potential). Embedded figures show atomic models for free energy calculation of bulk and surface structures.

the surface formation is attributed to the temperature dependency of material properties, such as E, in the K_G equation. Consequently, temperature effects are more significant for dislocation nucleation than for surface formation. This result is consistent with the conventional understanding of the difference in temperature effects on dislocation-based plastic deformation and crack-propagation-induced brittle fracture (analogous to the Yoffee diagram (Morris, 2011)).

Some experimental studies evaluated the activation volume of dislocation–GB interactions, which is expected to provide indirect insights into the mechanisms at play at the nanometer scale. For instance, the typical activation volume for the dislocation–GB interactions in ultrafine-grained chromium is $\sim 20b^3$ (Fritz et al., 2017). Comparing the experimental and simulated activation volumes is challenging because the activation volume is dependent on the grain size, as predicted by the Conrad model (Conrad, 2003). In the present atomistic study, an activation volume of $20b^3$ requires a high-stress state in BCC systems, as evident in Fig. 3(a) (e.g., more than 5 GPa of resolved shear stress for BCC Fe). This stress level is considerably higher than the macroscopic stress applied in experiments. The present atomistic simulations were conducted at 0 K using relatively small system sizes, whereas the experiments are at finite temperature, treating much larger length scales. Although there is a limitation of the direct comparison between the simulation result and experiments, one possible explanation of the predicted high-stress state from the activation volume is a stress concentration mechanism. Dislocation pile-up is a well-known mechanism of stress concentration and is related to the Hall–Petch relation between yield stress and grain size d (Hall, 1951; Petch, 1953; Pande et al., 1993; Fritz et al., 2017). This relationship suggests that dislocation transmission depends on grain size d because the stress concentration owing to the pile-up is affected by the grain size (or by the pile-up length or number of pile-up dislocations). Therefore, combination of atomistic knowledge for dislocation nucleation obtained in the present study and mesoscale modeling treating stress concentration caused by complex grain shape or dislocation pile-up should be promising approach to understand dislocation-based plastic deformation in realistic polycrystalline models.

The energy barrier for the dislocation nucleation from the surface is dominated by the self-energy of the nucleated dislocations in Fig. 5, although the energy changes at the surface also affect the activation energy. Fig. 5 treats dislocation nucleation with relatively large activation volume. When activation volume becomes small under high applied stress, the surface energy changes by dislocation nucleation (thus the surface structure) should affect dislocation nucleation. The realistic GB structures observed in experiments may intrinsically exhibit roughness or structural disorder owing to absorbed dislocations, steps (or offsets), and free volume. The roughness or structural disorder of experimental GBs should reduce the energy barrier for dislocation nucleation from GBs. The effect of GB structure or defects at the GBs on dislocation nucleation from GBs is an interesting and important topic, which is beyond the scope of the present study but will be investigated in detail in a future work.

5. Conclusions

In this study, we investigated dislocation nucleation from the surfaces of BCC metals using the FENEB method and via comparisons with the phenomenon observed for FCC metals. We also theoretically predicted the necessary shear stress of dislocation nucleation from planar faults at arbitrary temperatures and strain rates. We analyzed a frequency map for dislocation-related events and surface formation free energy as a function of temperature. The following major conclusions can be drawn from the findings of this study:

(i) The activation energies for dislocation nucleation in BCC metals obtained by FENEB depend on Burgers vector and shear modulus rather than the stacking fault energy and Peierls potential. This is different from the dislocation nucleation from FCC metals, which also depend on the stacking fault energy. This is attributed to the difference in their morphology of dislocation nucleation; in BCC metals, dislocation nucleation occurs from perfect dislocations, whereas in FCC metals, is originates from partial dislocations and the SF region.

(ii) The activation energies for the dislocation nucleation in BCC metals tend to be higher than those in FCC metals under similar resolved shear stresses. The edge and screw components in BCC metals exhibits similar activation energies and volumes of dislocation nucleation.
(iii) An atomistically-informed predictive model provides the temperature and strain-rate-dependent necessary stress for dislocation nucleation in BCC Fe. The predicted necessary stress for dislocation nucleation from planar faults at room temperature aligns with that obtained from experimental nanoindentation on GBs.
(iv) The calculated comparative frequency maps of kink-pair formation on screw-dislocation inner grains and dislocation nucleation from planar faults in BCC Fe provides the fundamentals of the dominant event of dislocation-related plastic deformation in metals.
(v) The free energy calculation method yields the temperature-dependent surface formation energy, which competes with dislocation nucleation under high-stress conditions, such as that at a crack tip.

These results provide significant insights into the dominant factors of dislocation nucleation, serving as the fundamental basis for modeling and tailoring the strength of BCC metals.

CRediT authorship contribution statement

Masato Wakeda: Writing – review & editing, Writing – original draft, Visualization, Validation, Resources, Project administration, Methodology, Investigation, Data curation, Conceptualization. **Tomohiro Ishigami:** Writing – review & editing, Validation, Methodology, Investigation. **Takahito Ohmura:** Writing – review & editing, Supervision, Resources, Project administration, Conceptualization.

Declaration of competing interest

The authors declare that they have no competing financial interests or personal relationships that may have influenced the work reported in this study.

Acknowledgment

Part of this work was supported by JST, PRESTO, Japan (Grant number JPMJPR219A), the Ministry of Education, Culture, Sport, Science and Technology of Japan (Grant Numbers JPMXP1122684766 and JPMXP1020230327), Japan and the Japan Society for the Promotion of Science KAKENHI (Grant Number 24H00389). M. W. is grateful to computational resources of supercomputer Fugaku provided by the RIKEN Center for Computational Science (Project ID: hp230212). Certain calculations in this study were performed using a numerical material simulator at the National Institute for Materials Science. M. W. is grateful to Mr. T. Arai (National Institute for Materials Science) for technical assistance.

Supplementary materials

Supplementary material associated with this article can be found, in the online version, at doi:10.1016/j.jmps.2026.106637.

Data availability

Data will be made available on request.

References

Aifantis, K.E., Deng, H., Shibata, H., et al., 2019. Interpreting slip transmission through mechanically induced interface energies: a Fe-3%Si case study. J. Mater. Sci. 54, 831–1843. https://doi.org/10.1007/s10853-018-2929-5.
Argon, A.S., Maloof, S.R., 1996. Plastic deformation of tungsten single crystals at low temperatures. Acta Metall. 14, 1449–1462. https://doi.org/10.1016/0001-6160(66)90165-9.
Blaschke, D.N., Szajewski, B.A., 2018. Line tension of a dislocation moving through an anisotropic crystal. Philos. Mag. 98 (26), 2397–2424. https://doi.org/10.1080/14786435.2018.1489152.
Conrad, H., 2003. Grain size dependence of the plastic deformation kinetics in Cu. Mater. Sci. Eng. 341, 216–228. https://doi.org/10.1016/S0921-5093(02)00238-1.
Fan, Y., Osetsky, Y.N., Yip, S., et al., 2012. Onset mechanism of strain-rate-induced flow stress upturn. Phys. Rev. Lett. 109, 135503. https://doi.org/10.1103/PhysRevLett.109.135503.
Freitas, R., Asta, M., Koning, M.D., 2016. Nonequilibrium free-energy calculation of solids using LAMMPS. Comput. Mater. Sci. 112, 333–341. https://doi.org/10.1016/j.commatsci.2015.10.050.
Fritz, R., Wimler, D., Leitner, A., et al., 2017. Dominating deformation mechanisms in ultrafine-grained chromium across length scales and temperatures. Acta Mater. 140, 176–187. https://doi.org/10.1016/j.actamat.2017.08.043.
Hall, E.O., 1951. The deformation and ageing of mild steel: III discussion of results. Proc. Phys. Soc. B 64, 747. https://doi.org/10.1088/0370-1301/64/9/303.
Hirth, J.P., Lothe, J., 1982. Theory of dislocations. Wiley, New York second ed.

Ito, K., Vitek, V., 2001. Atomistic study of non-Schmid effects in the plastic yielding of bcc metals. Phil. Mag. A 81, 1387–1407. https://doi.org/10.1080/01418610108214447.
Javaid, F., Pouriayevali, H., Durst, K., 2021. Dislocation-grain boundary interactions: recent advances on the underlying mechanisms studied via nanoindentation testing. J. Mater. Res. 36, 2545–2557. https://doi.org/10.1557/s43578-020-00096-z.
Kacher, J., Eftink, B.P., Cui, B., et al., 2014. Dislocation interactions with grain boundaries. Curr. Opin. Solid. State Mater. Sci. 18, 227–243. https://doi.org/10.1016/j.cossms.2014.05.004.
Kibey, S., Liu, J.B., Curtis, M.J., et al., 2006. Effect of nitrogen on generalized stacking fault energy and stacking fault widths in high nitrogen steels. Acta Mater. 54, 2991–3001. https://doi.org/10.1016/j.actamat.2006.02.048.
Koning, M.D., Antonelli, A., 1996. Einstein crystal as a reference system in free energy estimation using adiabatic switching. Phys. Rev. E 53, 465. https://doi.org/10.1103/PhysRevE.53.465.
Kraych, A., Clouet, E., Dezerald, L., et al., 2019. Non-glide effects and dislocation core fields in BCC metals. NPJ. Comput. Mater. 5, 109. https://doi.org/10.1038/s41524-019-0247-3.
Kuhr, B., Farkas, D., Robertson, I.M., 2016. Atomistic studies of hydrogen effects on grain boundary structure and deformation response in FCC Ni. Comput. Mater. Sci. 122, 92–101. https://doi.org/10.1016/j.commatsci.2016.05.014.
Kura, C., Wakeda, M., Hayashi, K., et al., 2022. Energetic and atomic structural analyses of the screw dislocation absorption at tilt grain boundaries in BCC-Fe. Sci. Rep. 12, 21301. https://doi.org/10.1038/s41598-022-25066-9.
Li, X., Schönecker, S., Vitos, L., et al., 2022. Generalized stacking faults energies of face-centered cubic high-entropy alloys: a first-principles study. Intermetallics 145, 107556. https://doi.org/10.1016/j.intermet.2022.107556.
Liang, Q., Weng, S., Fu, T., et al., 2022. Dislocation reaction-based formation mechanism of stacking fault tetrahedra in FCC high-entropy alloy. Mater. Chem. Phys. 282, 125997. https://doi.org/10.1016/j.matchemphys.2022.125997.
Ma, T., Kim, H., Mathew, N., et al., 2022. Dislocation transmission across Σ3{112} incoherent twin boundary: a combined atomistic and phase-field study. Acta Mater. 223, 117447. https://doi.org/10.1016/j.actamat.2021.117447.
Marinica, M.C., Ventelon, L., Gilbert, M.R., et al., 2013. Interatomic potentials for modelling radiation defects and dislocations in tungsten. J. Phys.:Condens. Matter 25 (39), 395502. https://doi.org/10.1088/0953-8984/25/39/395502.
McPhie, M.G., Berbenni, S., Cherkaoui, M., 2012. Activation energy for nucleation of partial dislocation from grain boundaries. Comput. Mater. Sci. 62, 169–174. https://doi.org/10.1016/j.commatsci.2012.05.039.
Mendelev, M.I., Han, S., Srolovitz, D.J., et al., 2003. Development of new interatomic potentials appropriate for crystalline and liquid iron. Phil. Mag. A 83 (35), 3977–3994. https://doi.org/10.1080/14786430310001613264.
Mishin, Y., Farkas, D., Mehl, M.J., et al., 1999. Interatomic potentials for monoatomic metals from experimental data and ab initio calculations. Phys. Rev. B 59 (5), 3393–3407. https://doi.org/10.1103/PhysRevB.59.3393.
Mishin, Y., Mehl, M.J., Papaconstantopoulos, D.A., et al., 2001. Structural stability and lattice defects in copper: ab initio, tight-binding, and embedded-atom calculations. Phys. Rev. B 63 (22), 224106. https://link.aps.org/doi/10.1103/PhysRevB.63.224106.
Mori, H., Ozaki, T., 2020. Neural network atomic potential to investigate the dislocation dynamics in bcc iron. Phys. Rev. Mater. 4, 040601. https://doi.org/10.1103/PhysRevMaterials.4.040601.
Mori, H., Tsuru, T., Okumura, M., et al., 2023. Dynamic interaction between dislocations and obstacles in bcc iron based on atomic potentials derived using neural networks. Phys. Rev. Matter. 7, 063605. https://doi.org/10.1103/PhysRevMaterials.7.063605.
Morris Jr, J.W., 2011. On the ductile-brittle transition in lath martensitic steel. ISIJ Int. 51, 1569–1575. https://doi.org/10.2355/isijinternational.51.1569.
Ohmura, T., Tsuzaki, K., Yin, F., 2005. Nanoindentation-induced deformation behavior in the vicinity of single grain boundary of interstitial-free steel. Mater. Trans. 46, 2026–2029. https://doi.org/10.2320/matertrans.46.2026.
Ohmura, T., Zhang, L., Sekido, K., et al., 2012. Effects of lattice defects on indentation-induced plasticity initiation behavior in metals. J. Mater. Res. 27, 1742–1749. https://doi.org/10.1557/jmr.2012.161.
Pan, Z., Rupert, T.J., 2014. Damage nucleation from repeated dislocation absorption at a grain boundary. Comput. Mater. Sci. 93, 206–209. https://doi.org/10.1016/j.commatsci.2014.07.008.
Pan, H., He, Y., Zhang, X., 2021. Interactions between dislocations and boundaries during deformation. Materials 14 (4), 1012. https://doi.org/10.3390/ma14041012.
Pande, C.S., Masumura, R.A., Armstrong, R.W., 1993. Pile-up based Hall-Petch relation for nanoscale materials. Nanostruct. Mater. 2 (3), 323–331. https://doi.org/10.1016/0965-9773(93)90159-9.
Petch, N.J., 1953. The cleavage strength of polycrystals. J. Iron Steel Inst. 174, 25–28.
Ravelo, R., Germann, T.C., Guerrero, O., et al., 2013. Shock-induced plasticity in tantalum single crystals: interatomic potentials and large-scale molecular-dynamics simulations. Phys. Rev. B 88 (13), 134101. https://doi.org/10.1103/PhysRevB.88.134101.
Rice, J.R., Thomson, R., 1974. Ductile versus brittle behavior of crystals. Philo. Mag. A 29, 73–97. https://doi.org/10.1080/14786437408213555.
Sato, Y., Shinzato, S., Ohmura, T., et al., 2019. Atomistic prediction of the temperature- and loading-rate-dependent first pop-in load in nanoindentation. Int. J. Plast. 121, 280–292. https://doi.org/10.1016/j.ijplas.2019.06.012.
Sekido, K., Ohmura, T., Hara, T., et al., 2012. Effect of dislocation density on the initiation of plastic deformation on Fe-C steels. Mater. Trans. 53, 907–912. https://doi.org/10.2320/matertrans.m2011356.
Shinzato, S., Wakeda, M., Ogata, S., 2019. An atomistically informed kinetic Monte Carlo model for predicting solid solution strengthening of body-centered cubic alloys. Int. J. Plast. 122, 319–337. https://doi.org/10.1016/j.ijplas.2019.03.004.
Song, J., Curtin, W.A., 2013. Atomic mechanism and prediction of hydrogen embrittlement in iron. Nat. Mater. 12, 145–151. https://doi.org/10.1038/nmat3479.
Spitzig, W., Keh, A., 1970. The effect of orientation and temperature on the plastic flow properties of iron single crystals. Acta Metall. 18, 611–622. https://doi.org/10.1016/0001-6160(70)90090-8.
Stukowski, A., Able, K., 2010. Extracting dislocations and non-dislocation crystal defects from atomistic simulation data. Modell. Simul. Mater. Sci. Eng. 18 (8), 085001. https://doi.org/10.1088/0965-0393/18/8/085001.
Stukowski, A., 2009. Visualization and analysis of atomistic simulation data with OVITO-the Open Visualization Tool. Modell. Simul. Mater. Sci. Eng. 18 (1), 015012. https://doi.org/10.1088/0965-0393/18/1/015012.
Suzudo, T., Ebihara, K., Tsuru, T., et al., 2022. Cleavages along {110} in bcc iron emit dislocations from the curved crack fronts. Sci. Rep. 12, 19701. https://doi.org/10.1038/s41598-022-24357-5.
Thompson, A.P., Aktulga, H.M., Berger, R., et al., 2022. LAMMPS - a flexible simulation tool for particle-based materials modeling at the atomic, meso, and continuum scales. Comp. Phys. Comm. 271, 10817. https://doi.org/10.1016/j.cpc.2021.108171.
Wakeda, M., Ohmura, T., 2023. Atomistic evaluation of the dislocation transmission across tilt and twist low-angle grain boundaries in body-centered cubic iron. Comput. Mater. Sci. 228, 112335. https://doi.org/10.1016/j.commatsci.2023.112335.
Wakeda, M., Tsuru, T., Kohyama, M., et al., 2017. Chemical misfit origin of solute strengthening in iron alloys. Acta Mater. 131, 445–456. https://doi.org/10.1016/j.actamat.2017.04.017.
Wakeda, M., Chang, Y.L., Ii, S., et al., 2021. Multiscale analyses of the interaction between dislocation and Σ9 symmetric tilt grain boundaries in Fe-Si bicrystals by nanoindentation technique. Int. J. Plast. 145, 103047. https://doi.org/10.1016/j.ijplas.2021.103047.
Wan, L., Geng, W.T., Ishii, A., et al., 2019. Hydrogen embrittlement controlled by reaction of dislocation with grain boundary in alpha-iron. Int. J. Plast. 112, 206–219. https://doi.org/10.1016/j.ijplas.2018.08.013.
Wang, M.G., Ngan, A.H.W., 2004. Indentation strain burst phenomenon induced by grain boundaries in niobium. J. Mater. Res. 19, 2478–2486. https://doi.org/10.1557/JMR.2004.0316.

Xu, S., Xiong, L., Chen, Y., et al., 2016. Sequential slip transfer of mixed-character dislocations across Σ3 coherent twin boundary in FCC metals: a concurrent atomistic-continuum study. NPJ. Comput. Mater. 2, 15016. https://doi.org/10.1038/npjcompumats.2015.16.

Yao, B.N., Liu, Z.R., Legut, D., et al., 2021. Cooperative roles of stacking fault energies on dislocation nucleation at bimetal interface through tunable potentials. Comput. Mater. Sci. 193, 110416. https://doi.org/10.1016/j.commatsci.2021.110416.

Zhang, J., Zhang, H., Ye, H., et al., 2016. Free-end adaptive nudged elastic band method for locating transition states in minimum energy path calculation. J. Chem. Phys. 145, 094104. https://doi.org/10.1063/1.4962019.

Zhang, Y., Ding, K., Stangebye, S., et al., 2022. Atomistic modeling of surface and grain boundary dislocation nucleation in FCC metals. Acta Mater. 237, 118155. https://doi.org/10.1016/j.actamat.2022.118155.

Zhao, Z., Safaei, B., Wang, Y., et al., 2022. Grain boundary elimination by twinning and dislocation nucleation in front of intergranular crack tips in BCC iron. Mater. Des. 215, 110515. https://doi.org/10.1016/j.matdes.2022.110515.